This work was carried out in whole or in part within the framework of the NOMATEN Center of Excellence, supported from the European Union Horizon 2020 research and innovation programme (Grant Agreement No. 857470) and from the European Regional Development Fund via the Foundation for Polish Science International Research Agenda PLUS programme (Grant No. MAB PLUS/2018/8).

This is a copy of the publication which appeared in: Materials Science and Engineering: A, vol 826, 141912, published on: 5 October 2021.

DOI: 10.1016/j.msea.2021.141912

Materials Science & Engineering A 826 (2021) 141912

Contents lists available at ScienceDirect

Materials Science & Engineering A

journal homepage: www.elsevier.com/locate/msea

Nanoindentation of single crystalline Mo: Atomistic defect nucleation and thermomechanical stability

F.J. Domínguez-Gutiérrez [a,b,*], S. Papanikolaou [a], A. Esfandiarpour [a], P. Sobkowicz [a], M. Alava [a,c]

[a] NOMATEN Centre of Excellence, National Centre for Nuclear Research, ul. A. Sołtana 7, 05-400 Swierk/Otwock, Poland
[b] Institute for Advanced Computational Science, Stony Brook University, Stony Brook, NY 11749, USA
[c] Department of Applied Physics, Aalto University, P.O. Box 11000, 00076 Aalto, Espoo, Finland

ARTICLE INFO

Keywords:
HT Nanoindentation
Dislocation dynamics
Molybdenum
Plastic deformation
Dislocation junctions
Thermomechanics

ABSTRACT

The mechanical responses of single crystalline Body-Centered Cubic (BCC) metals, such as molybdenum (Mo), outperform other metals at high temperatures, so much so that they are considered as excellent candidates for applications under extreme conditions, such as the divertor of fusion reactors. The excellent thermomechanical stability of molybdenum at high temperatures (400–1000 °C) has also been detected through nanoindentation, pointing toward connections to emergent local dislocation mechanisms related to defect nucleation. In this work, we carry out a computational study of the effects of high temperature on the mechanical deformation properties of single crystalline Mo under nanoindentation. Molecular dynamics (MD) simulations of spherical nanoindentation are performed at two indenter tip diameters and crystalline sample orientations [100], [110], and [111], for the temperature range of 10–1000 K. We investigate how the increase of temperature influences the nanoindentation process, modifying dislocation densities, mechanisms, atomic displacements and also, hardness, in agreement with reported experimental measurements. Our results suggest that the characteristic formation and high-temperature stability of [001] dislocation junctions in Mo during nanoindentation, in contrast to other BCC metals, may be the cause of the persistent thermomechanical stability of Mo.

1. Introduction

The development of novel technology in aerospace, electronic, medical and energy industries requires the use of materials that can mechanically sustain extreme operating conditions, that may include, among others, high temperature and irradiation. In these environments, it is characteristic that BCC metals, such as tungsten and molybdenum, display excellent features. For example, molybdenum is a material with persistent high temperature hardness and strength, as well as high resistance to corrosion [1–3], and good thermodynamic properties at high pressure [4–6]. These properties have promoted molybdenum to be used for building a plasma wall component and fusion divertors over other materials [2,7–10]. Nevertheless, compared to face-centered cubic (FCC) metals, the plastic behavior (strength, hardness) of BCC metals is quite complex and remains relatively unexplored, with only few nanoindentation studies addressing dislocation mechanisms in pure BCC single crystals [11–17]. In particular, it has remained poorly understood why some BCC metals display high thermomechanical stability at high temperatures, and persistence of mechanical properties. Especially, Mo single crystals display persistent hardness at high temperatures [18], a feature that is absent in other BCC single-crystalline metals [17]. While the emergence of such thermomechanical stability has previously been attributed to grain-boundary effects [19], in single crystals the effects shall be connected to fundamental dislocation mechanisms. Furthermore, the observation of corresponding thermomechanical stability in nanohardness, through nanoindentation, suggests the connection to defect nucleation [18]. Here, we investigate the mechanical nanoindentation response of Mo to a spherical indenter, at high temperatures, by using MD simulations, and considering [100], [110], and [111] orientations in a temperature range of 10–1000 K, and a repulsive imaginary indenter. Our results suggest that junction formation is prevalent in Mo, especially compared to other BCC metals, such as Ta [17] or W [14,20–22].

Temperature effects on plasticity of Mo have been shown to span a range of properties, from yield stress to the resistance to fatigue and creep to restrict progressive deformation [19,23]. Ab initio simulations have been used for the study beyond the point of maximum elastic deformation [24] and coupled atomistic continuum methods have been extensively used to simulate nanoindentation of Mo, concluding that plasticity mechanisms are consistent with typical mechanisms observed in other BCC metals [19,25,26]. In the context of BCC metals, studies of

* Corresponding author at: NOMATEN Centre of Excellence, National Centre for Nuclear Research, ul. A. Sołtana 7, 05-400 Swierk/Otwock, Poland.
E-mail address: javier.dominguez@ncbj.gov.pl (F.J. Domínguez-Gutiérrez).

https://doi.org/10.1016/j.msea.2021.141912
Received 17 May 2021; Received in revised form 10 August 2021; Accepted 14 August 2021
Available online 28 August 2021

nanoindentation in Ta [27] have shown that nanocontact plasticity in BCC is driven by the nucleation and propagation of twin and stacking fault bands, and Remington et al. showed that a cowboy-like "lasso" mechanism is responsible for the formation of prismatic loops [28]. In addition, the investigation of the temperature and loading-rate dependence of the first pop-in load in nanoindentation of Ta has provided further light to collective dislocation mechanisms [29]. A complementary dimension has been added through uniaxial compression studies of micropillars that showed the importance of the relative sample orientation and also, the key role of screw dislocations at room temperature in BCC metals (Ta, Mo and Fe), in contrast to FCC (Cu) [30,31]. Even though plasticity mechanisms in micropillar compression may be different than nanoindentation and quite complex [32], the key role of screw dislocations in driving plasticity in BCC metals cannot be understated. In this context, Molybdenum and its alloys are tougher than W facilitating the manufacturing process for the fusion machine components [9], where the mechanical properties such hardness and elastic modulus can be measured by nanoindentation [18,19,33–35] enabling to analyze thermal activated mechanisms that change the mechanical properties of the material. However, nanoindentation experiments at elevated temperatures have several technical issues that need to be considered, e.g. thermal drift that can be caused by a temperature mismatch between the tip and the sample [36].

A possible way to investigate features of nanomechanical properties and their causal relation to atomistic defect mechanisms at high temperatures, is through atomistic simulations. Molecular dynamics (MD) simulations have been extensively pursued in the past, showing to be a powerful tool toward emulating nanoindentation experiments, albeit at the nanoscale of few nanometers, while providing atomistic insights to the mechanical response of indented samples [26,27,29,37–39]. The major advantage of MD simulations at high temperatures is the ability to investigate the thermomechanical stability of dislocation nucleation and propagation, as well as stacking faults and twin boundaries, and how they contribute to the increase or decrease of hardness [40]. These atomistic simulations can also be applied to study the anisotropy of mechanical properties of materials at different temperatures which is a helpful tool to guide experiments where technical limits and costs are important [40,41].

In this work, we perform MD simulations to emulate nanoindentation of crystalline molybdenum by considering [100], [110], and [111] orientations in a temperature range of 10–800 K, with a spherical indenter. In Section 2 we describe the details of the numerical simulations. In Section 3, the atomistic insights of indentation processes in crystalline Mo sample are presented, where we track hardness as function of temperature, in conjunction to dislocation loop formation, local displacements' magnitude, and dislocation densities, showing the effects of sample temperatures on nanoindentation mechanisms. Agreement with experimental measurements is reported and discussed, in connection to dislocation junction formation. Finally, in Section 4, we provide concluding remarks.

2. Computational methods

In order to perform MD simulations of nanoindentation, the prepared sample is divided into three sections on the z direction for setting up boundary conditions, as shown in Fig. 1. In addition, we consider 5 nm vacuum section on the top, above the material sample and also the two lowest bottom layers are kept frozen ($\sim 0.02\times\mathbf{d}_z$) to assure stability of the Mo atoms when nanoindentation is performed. A thermostatic region above the already defined frozen one is considered to dissipate the generated heat during nanoindentation, with a thickness of $\sim 0.08\times\mathbf{d}_z$. The rest of the layers are defined as a region with dynamical atoms, in which the atoms interact as the indenter tip modifies the surface structure of the Mo sample. The dimensions of the simulation box, for the simulations performed in this work, are mentioned in Table 1.

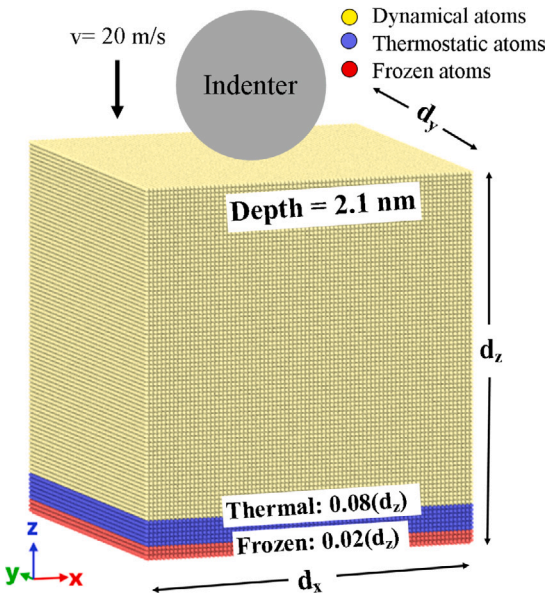

Fig. 1. (Color on-line). Schematic of the standard configuration in our MD simulations of Mo nanoindentation. The prepared Mo sample is divided into three regions to consider boundary conditions and a non-atomic repulsive spherical indenter is used.

Table 1
Simulation boxes sizes and number of Mo atoms.

Orientation	Size (d_x, d_y, d_z) [nm]	Atoms
[001]	25.18 $\hat{x}$ × 25.81 $\hat{y}$ × 26.90 $\hat{z}$	1 128 320
[110]	24.80 $\hat{x}$ × 25.44 $\hat{y}$ × 28.71 $\hat{z}$	1 171 170
[111]	26.21 $\hat{x}$ × 25.81 $\hat{y}$ × 30.10 $\hat{z}$	1 313 352

In the dynamical atoms region, the numerical modeling of a nanoindentation process starts by defining the simulation box as a pristine crystalline Mo sample based on a body-centered cubic cell. Then, we apply molecular dynamics through a NVE statistical thermodynamic ensemble, due to the high atomic mobility at elevated sample temperatures, where the velocity Verlet algorithm is implemented in the Large-scale Atomic/Molecular Massively Parallel Simulator (LAMMPS) software [38,42] Periodic boundary conditions are set on the x and y axes to simulate an infinite surface, while the z orientation contains a fixed bottom boundary and a free top boundary in all MD simulations.

The indenter tip is considered as a non-atomic repulsive imaginary (RI) rigid sphere with a force potential defined as: $F(t) = K\left(\vec{r}(t) - R\right)^2$ where $K = 236$ eV/Å^3 (37.8 GPa) is the force constant, and $\vec{r}(t)$ is the position of the center of the tip as a function of time, with radius R. Here, $\vec{r}(t) = x_0\hat{x} + y_0\hat{y} + (z_0 \pm \upsilon t)\hat{z}$ with x_0 and y_0 as the center of the surface sample on the xy plane, the $z_0 = 0.5$ nm is the initial gap between the surface and the indenter tip moves with a speed $\upsilon = 20$ m/s. The loading and unloading processes are defined by considering the direction of the velocity as negative and positive, respectively. Each process is performed for 125 ps with a time step of $\Delta t = 1$ fs. The maximum indentation depth is chosen to 2.1 nm to avoid the influence of boundary layers in the dynamical atoms region.

Our MD simulations are focused on standard nanoindentation simulations of body-centered cubic (BCC) molybdenum in the [100], [110], and [111] crystal orientations. For this, we use the LAMMPS software and utilize the embedded-atom method (EAM) potential [43,44] with a Finnis–Sinclair (FS) potential modification and a short interatomic distances corrections by repulsive Ziegler–Biersack–Littmark (ZBL) potential which realistically describes the strong repulsive forces at short ranges [44]. This interatomic potential can be utilized in our work due to the good agreement with experimental measurements for the threshold displacement energies E_d, melting temperature T_{melt}, and

surface binding energies U_s in the low index crystal directions [100], [110], and [111]. This leads to the well representation of SIA clusters (dumbbells and [111] crowdions) that is connected to dislocation formation and dynamics. The Mo samples are initially energy optimized at 0 K by the conjugate gradient algorithm with energy tolerance of 10^{-6} eV. The samples are then thermalized for 100 ps with a Langevin thermostat to temperatures of 10, 300, 600, 800 K and 1000 K with the time constant of 100 fs. This is done until the system reaches a homogeneous sample temperature and pressure profile. A final step is performed by relaxing the prepared sample for 10 ps to dissipate artificial heat. The EAM–FS–ZBL interatomic potential has been applied to study the formation of Frenkel pairs during collision cascades in our previous work [37], cascade morphology transition by Setyawan et al. [45], and used to validate experimental angular distributions of atoms sputtered from Mo samples by V.S. Chernysh et al. [46]. In order to validate that our MD simulations model correctly plastic deformation, we compute the elastic constants, C_{ij}, bulk modulus, and Poisson's ratio for different temperatures are computed by using the EAM potential for a small BCC Mo sample of 1 nm in the z direction. The obtained values are presented in Table 2.

2.1. Calculation of mechanical properties

The hardness of the indented sample is calculated by computing the $P-h$ curve with the Oliver and Pharr method [47], following the fitting curve to the unloading process curve as:

$$P = P_0 \left(h - h_f\right)^m \tag{1}$$

with P is the indentation load; h is the indentation depth and h_f is the residual depth after the whole indentation process; and P_0 and m are fitting parameters. Thus, the nanoindentation hardness can be computed as: $H = P_{\max}/A_c$ where $P_{\max}$ is the maximum indentation load at the maximum indentation depth, $A_c = \pi\left(2R - h_c\right)h_c$ is the projected contact area with R as the indenter tip radius and $h_c = h_{\max} - \epsilon P_{\max}/S$. Here $\epsilon = 0.75$ is a factor related to the spherical indenter shape, and unloading stiffness S is calculated as

$$S = \left(\frac{dP}{dh}\right)_{h=h_{\max}} = mP_0\left(h_{\max} - h_f\right)^{m-1}. \tag{2}$$

The Young's module E_Y is computed as:

$$\frac{1-\nu^2}{E_Y} = \frac{1}{E_r} - \frac{1-\nu_i^2}{E_i}, \tag{3}$$

where ν and ν_i are the Poisson's ratio of the Mo sample and indenter, respectively. E_i is the Young's modulus of the spherical indenter that is considered to be infinitely large, and the effective elastic modulus $E_r = \sqrt{\pi/A_c}S/2\beta$ with $\beta = 1$ for a spherical indenter shape. In this way, the nano-hardness of the indented samples can be calculated at different temperatures and indenter tip sizes.

Table 2
Elastic constants of molybdenum at various temperatures, obtained by MD simulations and compared with experimental values, in units of GPa. The lattice constant used in MD calculations is 3.1472 Å, based on a body-centered cube unit cell.

C_{ij}	MD	Exp.	MD	MD	MD
	0 K		300 K	600 K	800 K
C_{11}	464.7	464	417.8	354.1	321.6
C_{22}	464.7	464	409.3	340.5	307.6
C_{33}	464.7	464	415.3	347.9	312.9
C_{12}	161.5	159	163.2	163.2	162.5
C_{13}	161.5	159	163.3	164.7	165.1
C_{23}	161.5	159	162.2	160.5	159.8
C_{44}	108.9	109	108.4	108.3	108.3
C_{55}	108.9	109	107.0	104.2	102.4
C_{66}	108.9	109	106.1	102.1	99.5
Bulk Mod.	262.59	250	246.6	224.40	212.96
Poisson R.	0.26	0.29	0.28	0.32	0.34

The deformation of the indented Mo samples may be estimated through the use of the stress tensor σ_{ij}^n of the nth atom during the nanoindentation process. The von Mises stress of the nth atom is calculated as follows:

$$\sigma_{\text{Mises}}^n = \sqrt{\frac{3}{2}s_{ij}^n s_{ij}^n}, \quad \text{with} \quad s_{ij}^n = \sigma_{ij}^n - \frac{1}{3}\sigma_{kk}^n\delta_{ij}. \tag{4}$$

The six components of σ_{ij}^n are obtained from the output data of the MD simulations where the per-atom volume is defined by considering an elemental atomic volume (1 nm × 1 nm × 1 nm).

For the shear dependence of nanoindentation, atomic strains are computed through the distance difference, $\mathbf{d}^\beta$, between the mth nearest neighbors of the nth atom of the pristine and indented samples. Followed by defining the Lagrangian strain matrix of the nth atom as [39]:

$$\boldsymbol{\eta}_n = \quad 1/2\left(\boldsymbol{J}_n\boldsymbol{J}_n^T - I\right), \tag{5}$$

with

$$\boldsymbol{J}_n = \left(\sum_m \boldsymbol{d}_m^{0T}\boldsymbol{d}_m^0\right)^{-1}\left(\sum_m \boldsymbol{d}_m^{0T}\boldsymbol{d}_m\right). \tag{6}$$

Thus, the shear invariant of the nth atom is computed as:

$$\eta_n = \sqrt{\frac{\zeta_{ij}\zeta_{ij}}{2}}, \quad \text{with} \quad \zeta_{ij} = \eta_{ij} - \eta_{kk}\delta_{ij}. \tag{7}$$

This approach is implemented in OVITO [48].

3. Results

3.1. Temperature dependence of nano-hardness for [001], [110], and [111] orientations

The loading and unloading processes in nanoindentation of crystalline Mo oriented in [001], [110], and [111] are recorded, and the P–h curves are presented in Fig. 2 for a tip radius of 3 nm (for larger tip radius (6 nm), please see Section 3.2), at the different sample temperatures. At contact, all studied samples follow classical Hertz theory where the sphere–flat surface contact solution is expressed as

$$P^{hkl} = \frac{4}{3}\frac{E_Y^{hkl}}{1-\nu^2}R^{1/2}h^{3/2}, \tag{8}$$

where hkl are indexes related to the crystal orientation, ν is the Poisson's ratio, R is the indenter radius, h is the indenter displacement,

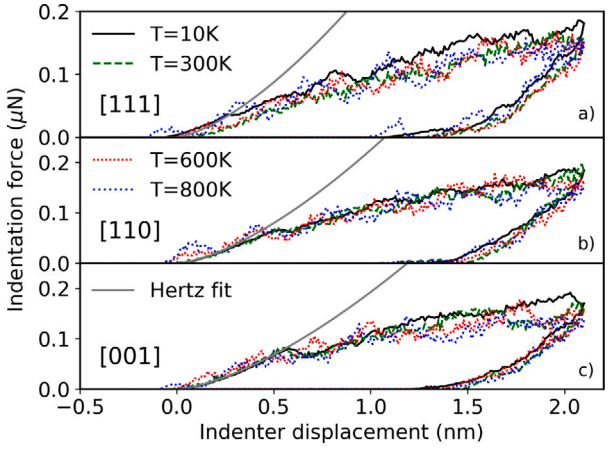

Fig. 2. (Color on-line). $P-h$ curve of the nanoindentation of crystalline Mo for the [111] in (a), [110] in (b), and [001] in (c) crystal orientations at 10 to 800 K sample temperatures for indenter radius 3 nm. A Hertz fitting curve, defined by Eq. (8), is added to the results at 10 K.

Table 3
Results obtained from MD simulation at the maximum indentation depth. Hardness, Young's modulus and yield stresses are presented in units of GPa. The mean pressure $\langle p_m \rangle$ is computed as the instance force divided by the contact area, A_c.

Orient.	[001]				[110]				[111]			
Temp. [K]	10	300	600	800	10	300	600	800	10	300	600	800
P_{max} [μN]	0.170	0.160	0.155	0.136	0.184	0.182	0.161	0.148	0.181	0.160	0.158	0.152
A_C [nm^2]	23.85	24.06	23.83	23.97	23.41	24.15	23.81	23.96	23.72	24.09	24.00	23.33
S [N/m]	432.5	461.76	387.87	424.42	369.3	504.54	403.27	301.29	416.9	456.27	399.8	317.81
H	6.92	6.59	6.28	6.38	7.23	6.84	6.60	4.57	7.12	6.40	5.89	6.43
E_Y	73.17	76.87	63.20	67.94	63.06	84.83	65.75	48.25	70.74	76.81	64.91	51.57
$\sigma_{\text{Hydro.}}$	−5.63	−6.23	−9.08	−10.79	−6.67	−7.20	−10.09	−14.31	−5.16	−5.27	−8.38	−12.39
σ_{Mises}	4.81	3.76	3.71	6.79	4.20	3.06	4.01	6.71	2.86	3.12	3.72	7.00
σ_{Tresca}	2.51	2.06	2.06	3.42	2.29	1.65	2.25	3.61	1.49	1.79	1.92	3.57
$\langle p_m \rangle$	7.13	6.63	6.50	5.71	7.86	7.53	6.76	6.18	7.63	6.64	6.58	6.51
$\frac{\sigma_{\text{Tresca}}}{\langle p_m \rangle}$	0.35	0.31	0.32	0.59	0.29	0.22	0.33	0.51	0.19	0.27	0.29	0.55

and E_Y^{hkm} is the elastic modulus calculated as

$$\frac{1}{E_Y^{hkl}} = S_{11} - 2\left[(S_{11} - S_{12}) - \frac{S_{44}}{2}\right] \times \left(\alpha^2\beta^2 + \alpha^2\gamma^2 + \beta^2\gamma^2\right), \quad (9)$$

with S_{ij} as the components of the compliance tensor and α, β, and γ are the direction cosines of the $[hkl]$ crystal orientation. Obtaining a elastic moduli of $E_Y^{001} = 381.39$ GPa, $E_Y^{110} = 287.02$ GPa, and $E_Y^{111} = 305.94$ GPa at the lowest temperature. It is observed that the deviation of MD simulations from the Hertzian elasticity solution at 10 K takes place at different deformations, greater than 0.57 ± 0.05 nm for [001], 0.5 ± 0.05 nm for [110], and 0.26 ± 0.05 nm for the [111] crystal orientation, consistent with experimental findings of orientation dependence in crystal plasticity of BCC metals [21,27,30].

We notice that the residual depth after indentation is $h_f = 1.4 \pm 0.1$ nm for [100] and [110] orientations, while a value of $h_f = 1.0$ nm is found for the [111] orientation at 10 K. When the sample is thermalized to 600 K, the elastic section of the P–h curve starts to oscillate due to the deformation of the surface shifting the residual depth after unloading process. This effect is more relevant at a temperature of 800 K, where the Mo atoms interact with the spherical indenter before touching the surface. We also notice that the indentation force at maximum depth, decreases as a function of the temperature, regardless of crystal orientations, in good agreement with reported results for Ta [27]. The plastic region of the curves show more oscillations at higher temperatures due to the thermal motion of dynamical atoms region in the sample.

The resulting P–h curve for the unloading process can be fitted to the Hertz elastic solution according to Eq. (1) to compute mechanical properties of the Mo sample like Hardness and Young's modulus, that should in principle compare to experimental data at comparable depths. In Table 3, we report the following values that are computed at the maximum indentation depth: maximum force, P_{max} in μN, the projected contact area, A_C in nm^2, the stiffness, S in units of N/m, and Hardness and Young modulus in units of GPa. As well as the hydrostatic stress $\sigma_{\text{Hydro.}} = (\sigma_{xx} + \sigma_{yy} + \sigma_{zz})/3$; the total value of von Mises and Tresca stresses; the mean pressure $\langle p_m \rangle$ is computed as the instance force divided by the contact area, A_c, namely F_{max}/A_C. We also verify the relation factor between the mean pressure and the maximum shear stress underneath the indenter, where the classical Hertz theory suggests a value of 0.465 (See Table 3). Our MD simulations corroborates that this factor depends on the atomic scale and sample temperature, as reported in the literature [49].

In order to provide more insights about the effect of temperature in the mechanical response of Mo samples, we analyze atomic strain information. This analysis provides information about the topography of surface deformation and pileup that can be compared to experimental results. In Fig. 3(a), we present the distribution of atomic displacement magnitude of damage of indented Mo samples in a top view for the [001] orientation with different sample temperatures, as an example. Noticing that pileups are found along the in-plane slip directions {101} and {10-1}, this region is gradually enlarged by increasing the temperature due to atomic thermal motion, commonly identified in BCC investigations [27].

In Fig. 3(b) and (c), we report the atomic shear strain and von Mises stress for different temperatures and the [001] orientation. The sample is slid to the half in the x axis to visualize the atomic distribution of the shear strain and von Mises stress by coloring Mo atoms according to their values. The increase of temperature suppresses propagation of dislocation lines, and suppresses the size of the plastic zone. It is also noticed that the strain and stress underneath the indenter increases as long as Mo atoms start moving faster due to thermal motion, which is also noted in the broader stress distribution. The analysis applied to the [110] and [111] crystal orientations are presented in the supplementary material (Appendix A). It is worth pointing out that the formation of a prismatic loop is observed on the [111] orientation at high temperatures, possibly suggesting that mechanisms shown at low temperatures [28] are relevant also at high temperatures.

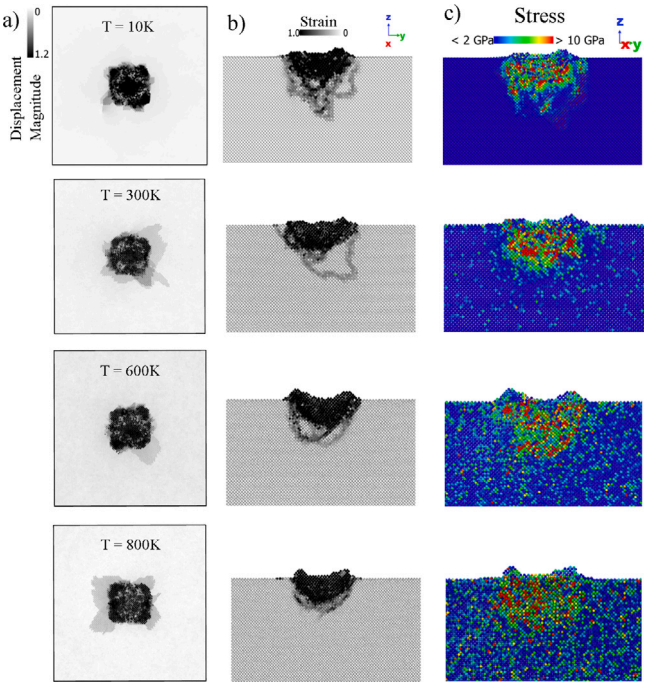

Fig. 3. Atomic analysis of the indented Mo sample at different temperatures at a depth of 2.1 nm for the [100] crystal orientation. Distribution of atomic displacement magnitude (in a range of 0–1 nm) on the top view is shown in (a). von Mises strain and stress beneath the indenter are presented in (b) and (c), respectively. (For interpretation of the references to color in this figure legend, the reader is referred to the web version of this article.)

It is interesting to analyze the atomic structure at the maximum indentation depth, where the computation and visualization of the dislocation structure are done by using the Dislocation Extraction Analysis (DXA) tool [48]. The output data provides the total length of dislocation lines and loops and their corresponding Burgers vectors. In Fig. 4(a), we present the formation of dislocation loops at the maximum nanoindentation depth in the [001] crystal orientation at a depth of 2.1 nm. In Fig. 4(b), the visualization of the deformed contact surface after unloading is shown, displaying the formation of pile-ups. We also include the information for the formation of shape and Burgers vector (depicted as blue arrows) of the $1/2\langle 111\rangle$ (colored in green), $\langle 100\rangle$ (colored in magenta), and $\langle 110\rangle$ (colored in blue) dislocations. The total length of the dislocations, L_T, is also noted, pointing to a dependence on the sample temperature after nanoindentation. In Fig. 4(b) we display the remained dislocations after unloading process where the effect of temperature is observed through the quick adsorption of dislocations on the sample surface. The effect of crystal orientation is reported in the supplementary material (Appendix A), where it is also shown that dislocations disappear after nanoindentation loads are removed at high temperatures.

3.2. Effect of the indenter tip radius

The spherical-tip nanoindentation studied in this work may resemble Berkovich nanoindentation at ultra-short depths (< 10 nm), however, in this regime, the mechanical response may display strong size effects [50], naturally influencing relevant plasticity mechanisms. The effects of the indenter tip size on the observed nanoindentation plasticity mechanisms of Mo samples, are tracked by considering a larger tip radius of 6 nm, followed by performing MD simulations under the same numerical environment as smaller tip ones. In Fig. 5, we present the P–h curve of the nanoindentation process at different sample temperatures and crystal orientations. The corresponding classical Hertz solution (Eq. (8)) is superposed to show the effects of the temperature during the interaction of the surface and the sphere. For this case, the MD simulations deviated from the Hertz elastic solution at 10 K at 0.86 ± 0.05 nm for [001], 0.78 ± 0.05 nm for [110], and 0.37 ± 0.05 nm for the [111] crystal orientation, also displaying very strong orientation dependence, as expected for BCC plasticity mechanisms [30]. Note that the first pop-in load is independent of the indenter size, leading to the [001] crystal orientation to reach the maximum indentation force and the [111] one to the lowest value regardless the sample temperature. Nevertheless, the pop-in load decreases from the [110] to [111] and [001] at temperatures above 600 K. We also note that the residual depth is 1.1 ± 0.05 nm for the three crystal orientations at 10 K. This value increases as function of the sample temperature. In Table 4, we report the obtained hardness H, Young modulus E_Y, stiffness S, and yield stresses σ as function of temperature for reference and further discussion.

In Fig. 6, we present the resultant atomic configuration of Mo samples after loading, as function of temperature for the [100] orientation, as an example. The analysis for the indented of Mo samples at [110] and [111] orientations are presented in the supplementary material of this work (Appendix A). In Fig. 6(a), we report the distribution of the atomic displacement magnitude in a scale of 0 to 1.2 nm. Here, the pileup pattern at 10 K shows expectedly that the maximum shear stress is observed for the {101} and {10-1} slip systems, as also reported for single crystalline Mo samples experimentally studied by Plummet et al. [18]. This stress pattern is maintained at higher temperatures. Fig. 6 shows the atomic strain and von Mises stress 6(b) and (c), respectively. While the thermally induced plastic zone reduction, observed for the smaller tip, is not present for the larger tip, there are close similarities to the atomic strain profiles and maxima as well as the temperature dependence of the von Mises stress.

In Fig. 7, the plastic zone is characterized in two limits: (a) at the maximum indentation depth and also, (b) after nanoindentation, and it is characterized through the identification of the types of emerging

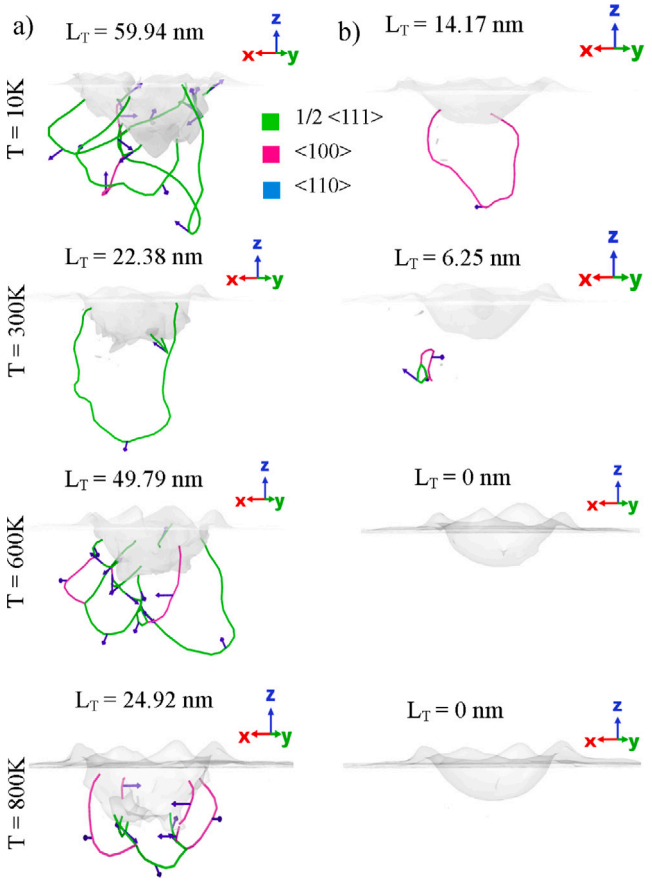

Fig. 4. Dislocation loops as a function of the indentation depth on the [001] orientation for different temperatures at the maximum indentation depth in (a) and after unloading process in (b). We also include information of the total length of the dislocation (L_T). Different types of dislocation loops are colored in green for $1/2\langle 111\rangle$, magenta for $\langle 100\rangle$, and blue for $\langle 110\rangle$. Burgers vector are displayed by blue arrows. (For interpretation of the references to color in this figure legend, the reader is referred to the web version of this article.)

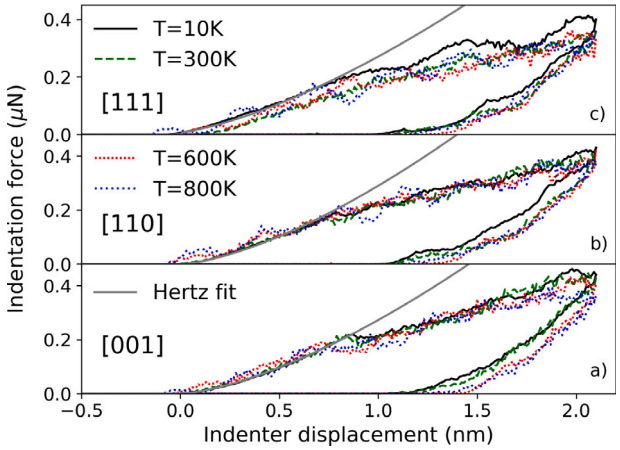

Fig. 5. (Color on-line). $P-h$ curve of the nanoindentation of crystalline Mo at a sample temperatures of 10 K to 800 K for the [001], [110], and [111] orientations for a indented tip radius of 6 nm. A Hertz fitting curve is added to graphs for both cases. Temperature effects on mechanical nanoindentation response are observed during the unloading process.

Table 4
Results obtained from MD simulation at the maximum indentation depth with an indentation size of 6 nm.

Orient.	[001]				[110]				[111]			
Temp. [K]	10	300	600	800	10	300	600	800	10	300	600	800
P_{max} [μN]	0.440	0.430	0.403	0.361	0.430	0.382	0.423	0.373	0.399	0.359	0.331	0.361
A_C [nm^2]	54.86	55.65	58.01	57.28	46.29	51.84	52.37	55.14	54.93	55.13	55.93	55.55
S [N/m]	781.37	849.71	1018.02	952.41	595.94	825.21	891.47	939.05	709.76	789.44	765.44	834.71
H	7.70	7.65	6.72	6.97	12.21	11.77	11.27	8.97	8.15	7.55	7.35	7.61
E_Y	87.17	93.03	106.32	109.06	72.38	96.71	97.99	99.12	80.27	86.83	89.58	87.78
$\sigma_{Hydro.}$	−15.66	−17.12	−19.63	−19.90	−11.38	−14.82	−17.07	−21.49	−11.62	−9.95	−14.33	−12.38
σ_{Mises}	7.58	4.54	1.26	4.05	8.16	5.69	2.49	4.53	8.33	5.71	1.71	7.00
σ_{Tresca}	3.92	2.45	0.70	2.14	4.27	3.16	1.42	2.47	4.36	2.92	0.99	3.58
$\langle p_m \rangle$	8.02	7.72	6.94	6.30	9.29	8.40	8.08	6.76	7.47	6.45	6.99	6.50
$\frac{\sigma_{Tresca}}{\langle p_m \rangle}$	0.49	0.32	0.1	0.34	0.46	0.38	0.18	0.36	0.58	0.45	0.17	0.55

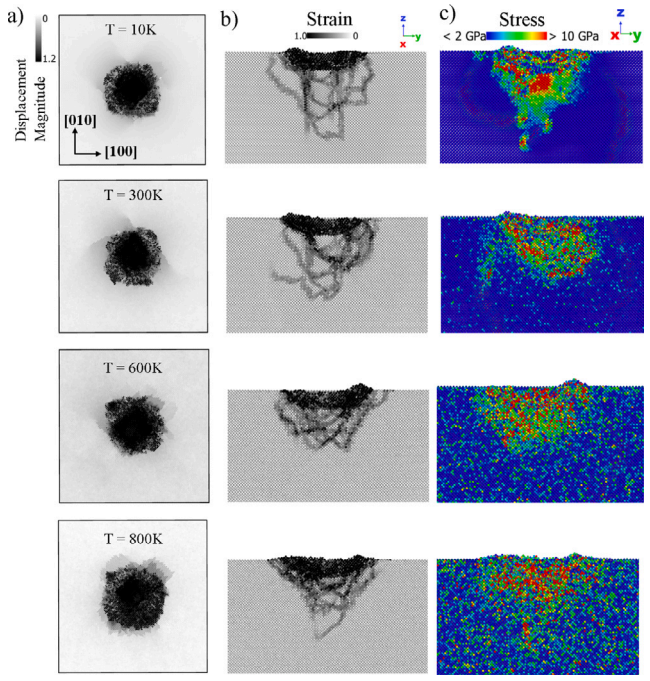

Fig. 6. (Color on-line) Analysis of the indented Mo sample for the [001] crystal orientation as function of the temperature by using a tip radius of 6 nm. Distribution of the atomic displacement magnitude is reported in (a), while von Mises strain and stress are shown in (b) and (c), respectively.

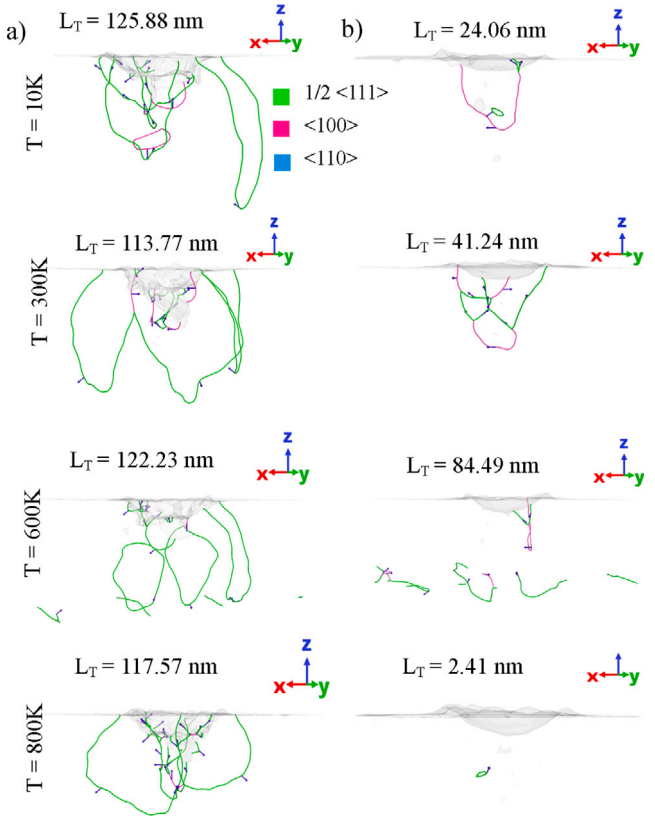

Fig. 7. Dislocations after maximum loading in (a) and after unloading process in (b) for Mo samples on the [100] orientation at different temperatures. The total length of the dislocation (L_T) is also presented. A radius of 6 nm is considered for the nanoindentation process. Color pattern follows the one used in Fig. 4. (For interpretation of the references to color in this figure legend, the reader is referred to the web version of this article.)

dislocations at different temperatures. During loading, it is observed that the total length of the dislocations is larger than those reported for a smaller indenter regardless of the sample temperature. Evidence of the 'lasso' mechanism [28] exists at all temperatures, suggesting that the main dislocation nucleation mechanism remains analogous to other BCC metals. After unloading, there is evidence of remaining dislocations that provide clues for the hardening mechanisms at high temperatures. Only at 800 K the dislocation nucleation appears to be overwhelmed by thermal atomic motions that drive dislocations toward surface deposition events. The formation of prismatic loops is favorable for large radius indenters at all temperatures (up to 800 K), justifying prior studies for other BCC metals.

3.3. MD insights for experiments in Mo

In Fig. 8 we present the temperature dependence of hardness of Mo on the [001] orientation at 2.1 nm depth and its comparison to experimental data reported by Plummer et al. [18] for the same crystal orientation. We also include experimental data of Mo by Pisarenko et al. [22] and Minnert et al. [35] for polycrystalline Mo samples as reference. We finally include the experimental measurements by Terentyev et al. [20] for W showing a monotonically decrease of hardness as a function of the temperature. The high temperature behavior resembles the one observed in the experiments [18,22,35] where the material hardness reaches a saturation at a temperature of ~ 700 K. This is encouraging, given that the experimentally studied depths were much larger, pointing toward maintaining the same trend in thermal effects, despite the strong size effects. This finding is consistent with successfully modified Nix–Gao models that suggest that the emergence of thermal effects arises only through the statistically stored dislocation density in the plastic zone and in a power law form, which is then linearly added to the geometrically necessary dislocation density [19,51]. The considered error bars in hardness are obtained through additional MD simulations and computed as $\sigma = \sqrt{\sum_i (x_i - \langle H \rangle)/N}$ is the standard deviation, $\langle H \rangle$ the average of the MD results, and $N = 5$,

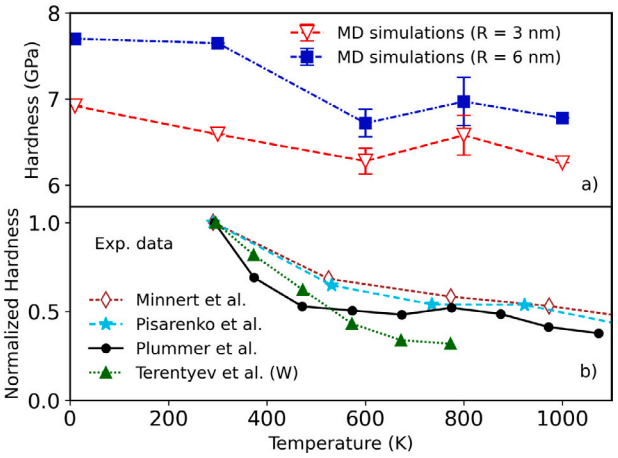

Fig. 8. (Color on-line). Hardness as a function of temperature for the [100] orientation at a depth of 2.1 nm in (a) and comparison to experimental measurements in (b) reported by Plummer et al. [18], Pisarenko et al. [22], Minnert et al. [35]. For comparison, we show experimental data for W by Terentyev et al. [20] showing a monotonic decrease of the material hardness as function of temperature.

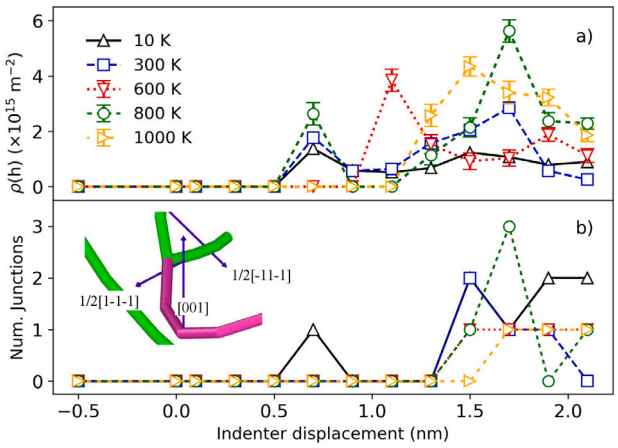

Fig. 10. Dislocation density in (a) and number of [001] junctions in (b) as function of the indenter displacement for several temperatures, for an indenter radius of 3 nm and a [001] crystal orientation. Besides the effect of the temperature on the mechanical nanoindentation response, we observed the formation of dislocation junctions in the sample making it to increase its hardness, as shown in (b). As an example, we show the dislocation junction in the inset of the figure (b) where the [001] dislocation is produced by two 1/2[111] dislocations which is the more energetically favorable [52] and thermodynamically stable once formed [53]. (For interpretation of the references to color in this figure legend, the reader is referred to the web version of this article.)

the total number of MD simulations performed. As an example, Fig. 9 shows the P–h curves of the nanoindentation of the sample at 800 K for a radius of 3 nm in (a) and 6 nm in (b) where the increase of the hardness material is observed.

The thermomechanical stability seen in the hardness data (see Fig. 8) is strongly correlated with the total dislocation length and dislocation propagation during nanoindentation. In Fig. 10(a) we show the dislocation density as function of the indenter displacement for different temperatures by considering the 3 nm-sized indenter tip. The results for the bigger indenter tip are also presented in the supplementary material (Appendix A). By using the approximations of a spherical plastic zone, the dislocation density, ρ(h) is computed as

$$\rho(\mathrm{h}) = \mathrm{L_T}\left[\frac{2\pi}{3}\left(R_{pl}^3 - h^3\right)\right]^{-1}, \tag{10}$$

where $\mathrm{L_T}$ is the dislocation length, and R_{pl} is the largest distance of a dislocation measured from the indentation displacement, considering a hemispherical geometry. From our MD simulations, we observe (see Fig. 10a) that the nucleation of $b = 1/2[111]$ and $b = [001]$ dislocations is responsible for the hardness saturation at high temperatures. This result is in good agreement with those reported by S. Aubry et al. [54], at elevated temperatures the energy difference between the [001] and [111] dislocations decreases for α Fe, showing that dislocations with **b** = [001] start to lead the plastic deformation for BCC materials, as temperature increases.

Moreover, as shown in the inset of Fig. 10(b), the [001] dislocation segments are actually, dislocation junctions between 1/2[1-1-1] and 1/2[-11-1] dislocations, as well as their symmetry equivalents which is the more energetically favorable junction [52] and thermodynamically stable once formed [53]. The number of this type of junctions found in our MD simulations as a function of the indenter displacement is presented in Fig. 10(b) and its schematic is displayed in the inset. Here Burgers vectors are depicted as blue arrows and dislocation lines are shown by green and pink lines for 1/2[111] and [001], respectively. In the supplementary material, we also show a visualization of dislocation nucleation as function of time for the [001] Mo sample at different temperatures to demonstrate the generic formation of [001] junctions (Appendix A). These junctions are proliferating at high temperatures, and are highly stable at the maximum load. The screw [001] dislocation junctions have been long considered as a major hardening mechanism in BCC metals [55,56]. Where in principle it can glide in any plane of its Burgers vector zone, which does not coincide with the slip plane of the material, increasing the strain hardening of the material [57,58] that may explain typical strengthening due to the mobility of screw dislocations is comparatively very low but strongly temperature-dependent. [59,60].

Thus, we suggest that [001] junctions may be responsible for the persistent thermomechanical stability of Mo single crystals. Thermally stable [001] junctions are found to be responsible for increasing material nanohardness, and in contrast, this kind of junction formation has been shown to be unstable in other BCC metals, such as W and Ta [20,27]. We conclude that the combination of kinetics and energetics in molybdenum leads to an increased stability of [001] junctions that are well known to play key role in strengthening effects of BCC metals [55].

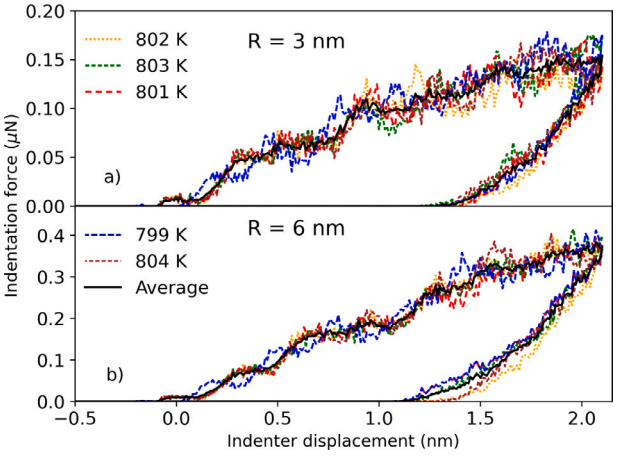

Fig. 9. (Color on-line). P–h curve of the nanoindentation of [001] Mo at 800 K by considering different thermalized samples for an indenter tip of 3 nm in (a) and 6 nm in (b). The average of the Load as a function of the indention depth is included and computed as $\langle \mathrm{P}(h)\rangle = 1/N \sum_k^N \mathrm{P}(h)_k$ with N = 5 as the number of the MD simulations.

4. Concluding remarks

In this work, we performed MD simulations to investigate the thermal stability of the mechanical response of crystalline molybdenum

during nanoindentation, investigating the effects of crystal orientation, temperature and dislocation mechanisms. We characterized the nanoindentation process in molybdenum, in connection to experimental findings, and through tracking strain accumulation and dislocation mechanisms for several temperatures, sample orientations and indenter tips. Our simulation results suggest that crystal plasticity in nanoindentation of molybdenum follows closely known defect nucleation mechanisms for BCC metals, albeit with distinct differences in the formation and thermal stability of [001] junctions, that are observed and quantified as function of temperature during loading. The observed [001] junction formation in molybdenum was shown to be responsible for increasing the nano-hardness of molybdenum, by correlating it to the dislocation density of each dislocation type. In contrast, such stable junction formation is barely observed during nanoindentation of W and Ta [20,27]. Given that [001] junctions are well known culprits of hardening in BCC metals [55], we believe that persistent high-temperature hardness in Mo may be attributed to [001] junction formation. Therefore, the simulation results presented in this work suggest that there may be fundamental dislocation-based kinetic reasons for molybdenum being a good, low-maintenance material candidate for applications in extreme environmental conditions, over other BCC metals.

CRediT authorship contribution statement

F.J. Domínguez-Gutiérrez: Conception and design of study, Acquisition of data, Analysis and/or interpretation of data, Writing – original draft, Writing – review & editing. **S. Papanikolaou:** Conception and design of study, Analysis and/or interpretation of data, Writing – original draft, Writing – review & editing. **A. Esfandiarpour:** Analysis and/or interpretation of data, Writing – original draft. **P. Sobkowicz:** Analysis and/or interpretation of data, Writing – original draft, Writing – review & editing. **M. Alava:** Conception and design of study, Analysis and/or interpretation of data, Writing – original draft, Writing – review & editing.

Declaration of competing interest

The authors declare that they have no known competing financial interests or personal relationships that could have appeared to influence the work reported in this paper.

Acknowledgments

We would like to thank Łukasz Kurpaska for inspiring conversations. We acknowledge support from the European Union Horizon 2020 research and innovation program under grant agreement no. 857470 and from the European Regional Development Fund via the Foundation for Polish Science International Research Agenda PLUS program grant No. MAB PLUS/2018/8. We acknowledge the computational resources provided by the High Performance Cluster at the National Centre for Nuclear Research in Poland, and also the Seawulf institutional cluster at the Institute for Advanced Computational Science in Stony Brook University.

All authors approved the version of the manuscript to be published.

Appendix A. Supplementary material

We provide the analysis of the indented Mo sample for the [110] and [111] at different temperatures and indenter size. As well as the visualization of the dislocation loops at the maximum indentation depth and after unloading process.

Supplementary material related to this article can be found online at https://doi.org/10.1016/j.msea.2021.141912.

References

[1] K.M. Xue, Z. Wang, X. Wang, Y.F. Zhou, P. Li, Mater. Sci. Technol. (2020) 1–9.
[2] S. Lee, K. Edalati, Z. Horita, Mater. Trans. 51 (2010) 1072–1079.
[3] L. Hollang, D. Brunner, A. Seeger, Mater. Sci. Eng: A 319–321 (2001) 233–236.
[4] K.D. Litasov, P.I. Dorogokupets, E. Ohtani, Y. Fei, A. Shatskiy, I.S. Sharygin, P.N. Gavryushkin, S.V. Rashchenko, Y.V. Seryotkin, Y. Higo, K. Funakoshi, A.D. Chanyshev, S.S. Lobanov, J. Appl. Phys. 113 (2013) 093507.
[5] E.C. Ragan III., M.G. Silbert, B.C. Diven, J. Appl. Phys. 48 (1977) 2860–2870.
[6] I. Cieszykowska, T. Janiak, T. Barcikowski, Appl. Radiat. Isot. 124 (2017) 124–131.
[7] P. Li, Q. Lin, X. Wang, Y. Tian, K.M. Xue, Int. J. Refract. Met. Hard Mater. 72 (2018).
[8] A. Kumar, B.L. Eyre, J.W. Christian, Proc. R. Soc. Lond. Ser. A Math. Phys. Eng. Sci. 370 (1980) 431–458.
[9] M. Budd, J. Nucl. Mater. 170 (1990) 129–133.
[10] The divertor, 2021, https://www.iter.org/mach/divertor (accessed: 15/2/2021).
[11] R. Smith, D. Christopher, S.D. Kenny, A. Richter, B. Wolf, Phys. Rev. B 67 (2003) 245405.
[12] K. Durst, B. Backes, O. Franke, M. Göken, Acta Mater. 54 (2006) 2547–2555.
[13] N. Stelmashenko, M. Walls, L. Brown, Y.V. Milman, Acta Metall. Mater. 41 (1993) 2855–2865.
[14] S. Syed Asif, J. Pethica, Phil. Mag. A 76 (1997) 1105–1118.
[15] D.F. Bahr, D.E. Kramer, W. Gerberich, Acta Mater. 46 (1998) 3605.
[16] D. Kramer, K. Yoder, W. Gerberich, Phil. Mag. A 81 (2001) 2033–2058.
[17] M.M. Biener, J. Biener, A.M. Hodge, A.V. Hamza, Phys. Rev. B 76 (2007) 165422.
[18] K.P. Plummer, The Temperature Dependence of Plasticity in Molybdenum (Ph. D. dissertation), University of Oxford, 2021.
[19] G.Z. Voyiadjis, A.H. Almasri, T. Park, Mech. Res. Commun. 37 (2010) 307–314.
[20] D. Terentyev, X. Xiao, S. Lemeshko, U. Hangen, E. Zhurkin, Int. J. Refract. Met. Hard Mater. 89 (2020) 105222.
[21] B.D. Beake, S. Goel, Int. J. Refract. Met. Hard Mater. (ISSN: 0263-4368) 75 (2018) 63–69, URL https://www.sciencedirect.com/science/article/pii/S026343681830060X.
[22] G. Pisarenko, V. Borisenko, Y. Kashtalyan, Powder Metall. Met. Ceram. 1 (1964) 371.
[23] J. Braun, L. Kaserer, J. Stajkovic, K.H. Leitz, B. Tabernig, P. Singer, P. Leibenguth, C. Gspan, H. Kestler, G. Leichtfried, Int. J. Refract. Met. Hard Mater. 84 (2019) 104999.
[24] W. Luo, D. Roundy, M.L. Cohen, J.W. Morris, Phys. Rev. B 66 (9) (2002) 094110.
[25] R. Picu, J. Comput.-Aided Mater. Des. 7 (77) (2000).
[26] J. Hu, M. Li, W. Wang, L. Li, Molecular Dynamics Simulations on Nanoindentation Experiment of Single-Layer Mos2 Circular Nanosheets Advanced Mechanical Science and Technology for the Industrial Revolution 4.0, Springer Singapore, Singapore, ISBN: 978-981-10-4109-9, 2018, pp. 333–339,
[27] J. Alcalá, R. Dalmau, O. Franke, M. Biener, J. Biener, A. Hodge, Phys. Rev. Lett. 109 (7) (2012) 075502, URL https://link.aps.org/doi/10.1103/PhysRevLett.109.075502.
[28] T. Remington, C.J. Ruestes, E.M. Bringa, B.A. Remington, C. Lu, B. Kad, M.A. Meyers, Acta Mater. 78 (2014) 378–393.
[29] Y. Sato, S. Shinzato, T. Ohmura, S. Ogata, Int. J. Plast. 121 (2019) 280–292, URL https://www.sciencedirect.com/science/article/pii/S0749641919302335.
[30] D. Kaufmann, A.S. Schneider, R. Mönig, C.A. Volkert, O. Kraft, Int. J. Plast. 49 (2013) 145–151, URL https://www.sciencedirect.com/science/article/pii/S0749641913000740.
[31] D. Kaufmann, R. Mönig, C.A. Volkert, O. Kraft, Int. J. Plast. 27 (2011) 470–478, URL https://www.sciencedirect.com/science/article/pii/S0749641910001130.
[32] S. Papanikolaou, Y. Cui, N. Ghoniem, Modelling Simulation Mater. Sci. Eng. 26 (2017) 013001.
[33] G.Z. Voyiadjis, M. Yaghoobi, Crystals 7 (321) (2017).
[34] J. Zhao, P. Huang, K. Xu, F. Wang, T. Lu, Thin Solid Films 653 (2018) 365–370.
[35] C. Minnert, W.C. Oliver, K. Durst, Mater. Des. 192 (2020) 108727.
[36] J. Wheeler, D. Armstrong, W. Heinz, Schwaiger R., Curr. Opin. Solid State Mater. Sci. 19 (2015) 354–366.
[37] F.J. Domínguez-Gutiérrez, J. Byggmästar, K. Nordlund, F. Djurabekova, U. von Toussaint, Model. Simul. Mater. Sci. Eng. (2021) URL http://iopscience.iop.org/article/10.1088/1361-651X/abf152.
[38] S. Plimpton, J. Comput. Phys. 117 (1995) 1–19.
[39] F. Shimizu, S. Ogata, J. Li, Mater. Trans. 48 (2007) 2923–2927.
[40] S. Lee, A. Vaid, J. Im, et al., Nature Commun. 11 (2020) 2367.
[41] D. Christopher, R. Smith, A. Richter, Nanotechnology 12 (2001) 372–383, URL https://doi.org/10.1088/0957-4484/12/3/328.
[42] D. Frenkel, B. Smit, Understanding Molecular Simulation: From Algorithms to Applications, Vol. 1, Elsevier, ISBN: 0080519989, 2001.
[43] G.J. Ackland, R. Thetford, Phil. Mag. A 56 (1987) 15–30.
[44] E. Salonen, T. Järvi, K. Nordlund, J. Keinonen, J. Phys.: Condens. Matter 15 (2003) 5845–5855.
[45] W. Setyawan, A.P. Selby, N. Juslin, R.E. Stoller, B.D. Wirth, R.J. Kurtz, J. Phys.: Condens. Matter 27 (2015) 225402, URL https://doi.org/10.1088/0953-8984/27/22/225402.

[46] V. Chernysh, A. Ieshkin, D. Kireev, A. Nazarov, A. Zavilgelsky, Surf. Coat. Technol. (ISSN: 0257-8972) 388 (2020) 125608, URL https://www.sciencedirect.com/science/article/pii/S0257897220302772.
[47] W. Oliver, G. Pharr, J. Mater. Res. 7 (1992) 1564–1583.
[48] A. Stukowski, Modelling Simulation Mater. Sci. Eng. (ISSN: 0965-0393) 18 (2010).
[49] S. Goel, B. Beake, C.W. Chan, N. Haque Faisal, N. Dunne, Mater. Sci. Eng. A 627 (2015) 249–261.
[50] R. Bolin, H. Yavas, H. Song, K.J. Hemker, S. Papanikolaou, Crystals 9 (652) (2019).
[51] H. Song, H. Yavas, E. Van der Giessen, S. Papanikolaou, J. Mech. Phys. Solids 123 (2019) 332–347.
[52] P. Munroe, I. Baker, Acta Metall. Mater. (ISSN: 0956-7151) 39 (1991) 1011–1017, URL https://www.sciencedirect.com/science/article/pii/095671519190302H.
[53] N. Gao, Z. Yao, G. Lu, et al., Nat. Commun. 12 (2021) 225.
[54] S. Aubry, S.P. Fitzgerald, S.L. Dudarev, W. Cai, Modelling Simulation Mater. Sci. Eng. 19 (2011) 065006, URL https://doi.org/10.1088/0965-0393/19/6/065006.
[55] A. Argon, Strengthening Mechanisms in Crystal Plasticity, Vol. 4, Oxford University Press on Demand, ISBN: 0198516002, 2008.
[56] K. Arakawa, T. Amino, H. Yasuda, H. Mori, ISIJ Int. 57 (2017) 2065–2069.
[57] N. Bertin, W. Cai, S. Aubry, V.V. Bulatov, Phys, Rev. Mater. 5 (2) (2021) 025002, URL https://link.aps.org/doi/10.1103/PhysRevMaterials.5.025002.
[58] G.A. Malygin, Phys. Status Solidi (A) 119 (1990) 423–436.
[59] R.B. Sills, N. Bertin, A. Aghaei, W. Cai, Phys. Rev. Lett. 121 (8) (2018) 085501, URL https://link.aps.org/doi/10.1103/PhysRevLett.121.085501.
[60] L. Kubin, B. Devincre, M. Tang, J. Comput.-Aided Mater. Des. 5 (31) (1998).